Front. Mech. Eng. 2023, 18(4): 49
https://doi.org/10.1007/s11465-023-0765-z

RESEARCH ARTICLE

Multi-material additive manufacturing—functionally graded materials by means of laser remelting during laser powder bed fusion

Alexander SCHMIDT (✉), Felix JENSCH, Sebastian HÄRTEL

Chair of Hybrid Manufacturing, Brandenburg University of Technology, Cottbus 03046, Germany
✉ *Corresponding author. E-mail: alexander.schmidt@b-tu.de (Alexander SCHMIDT)*

ABSTRACT Many processes may be used for manufacturing functionally graded materials. Among them, additive manufacturing seems to be predestined due to near-net shape manufacturing of complex geometries combined with the possibility of applying different materials in one component. By adjusting the powder composition of the starting material layer by layer, a macroscopic and step-like gradient can be achieved. To further improve the step-like gradient, an enhancement of the *in-situ* mixing degree, which is limited according to the state of the art, is necessary. In this paper, a novel technique for an enhancement of the *in-situ* material mixing degree in the melt pool by applying laser remelting (LR) is described. The effect of layer-wise LR on the formation of the interface was investigated using pure copper and low-alloy steel in a laser powder bed fusion process. Subsequent cross-sectional selective electron microscopic analyses were carried out. By applying LR, the mixing degree was enhanced, and the reaction zone thickness between the materials was increased. Moreover, an additional copper and iron-based phase was formed in the interface, resulting in a smoother gradient of the chemical composition than the case without LR. The Marangoni convection flow and thermal diffusion are the driving forces for the observed effect.

KEYWORDS multi-material additive manufacturing (MMAM), functionally graded materials (FGMs), laser powder bed fusion (L-PBF), laser remelting (LR), pure copper

1 Introduction

Functionally graded materials (FGMs) are characterized by either a continuous or targeted discrete change in the chemical composition and microstructure, and thus, graded thermophysical properties of the parts. The benefit of FGM is overcoming the limitations of dissimilar metal joints resulting from interfacial stresses or chemical incompatibility by a continuous gradient while combining the respective advantages of different materials, resulting in superior part properties. According to literature, production technologies, such as casting, sintering, powder metallurgy, diffusion bonding, thermal spraying, and physical or chemical vapor deposition, may be used for manufacturing FGM [1–5]. Each of the mentioned technology shows advantages and limitations.

Technologies such as thermal spraying and physical or chemical vapor deposition are processes used for economical production of functional coatings on part surfaces but not complete parts. Here, a layer-wise deposition of different materials by the respective technology is conducted. Compared with additive manufacturing (AM), the material deposition of the coating technologies is not local, and the material thickness is generally limited up to a few hundred microns. The production of graded near-net shape parts is not economical nor possible because of the low deposition rates for the case of chemical and physical vapor deposition or the process workflow and characteristics. For the case of diffusion bonding, a gradient can be achieved by bonding two or more parts of different materials. The gradient results from the diffusion of the materials. By diffusion bonding, high-quality bonds of even materials with different thermophysical characteristics are possible. Since diffusion bonding is an additional process step in the production chain and diffusion-driven material transport is time consuming, the economic efficiency of the whole production chain is limited. In casting processes, such as controlled mold

---

Received March 8, 2023; accepted July 20, 2023

filling, two different materials in liquid state are used for manufacturing a gradient. In the first step, the mold is filled with the first material melt. After partial solidification, the second material melt is casted on top. The advantage of such a process is high productivity and the unlimited size of the parts. The disadvantage is the limited geometrical complexity of the parts. Sintering and powder metallurgy are original forming processes with ceramic or metal powder as feedstock material. A geometrical defined part is formed by solid-state consolidation or partially liquid phase sintering of the preform. The partially liquid phase sintering and consolidation processes take place due to diffusion resulting from high temperature and high mechanical or gas pressure load, and they are accompanied by densification and thus a volume loss of the preform. In both cases, a gradient is achieved by local adjustment of the chemical composition of the preform. For the case of powder metallurgy by means of hot isostatic pressing of encapsulated powder, complex 3D parts with graded chemical composition are possible. Due to the preform volume loss, the challenge is the design of the preform resulting in a near-net-shaped part with complex geometry after the respective process, particularly for the case of different materials with different consolidation and densification behavior, and different thermomechanical properties. Moreover, due to densification and thus a possible shift of the powder layers to each other, the gradient may be formed in an undesired direction.

Multi-material additive manufacturing (MMAM) increasingly attracts the industry and academia because of its numerous technological advantages, such as near-net shape manufacturing of complex geometries with hollow structures and the FGM promising possibility of applying different materials in one component [6,7]. According to the state of the art, several AM processes are suited for manufacturing a step-like gradient.

For the case of a laser-directed energy deposition (L-DED) with powder process, the feedstock material is deposited into the laser focus on the substrate surface by a powder nozzle. The feedstock material fuses by melting and thus forms a geometrically defined part during solidification. Considering contemporary L-DED with powder devices have several powder feeders and nozzles around the laser focus, adjusting the chemical composition layer-wise is possible by pre-blending the powder before the process or blending the powder *in-situ* in the laser focus. Knoll et al. [8], Li et al. [9], Domack and Baughman [10], and Ocylok et al. [11] applied this approach successfully to produce different multi-material parts. With regard to the middle of each layer, this approach resulted in a successful gradient of the chemical composition. Concerning the respective layer interfaces, the transition of chemical composition was not continuous but discrete. Such an interface might be crucial for some material combinations due to interfacial stresses and chemical incompatibility.

Powder bed fusion (PBF) processes spread the powder uniformly on the bed platform by means of a hopper and, depending on the specific technology, a roller or a blade. Afterwards, the powder is melted locally along the scan path by the heat source, which can be a laser or an electron beam. Due to the melting, the powder fuses locally and thus forms a geometrically defined part during solidification. Considering the powder around the part is not melted, it may be used further for manufacturing other geometries if different powders are not mixed and if the one-time used powder meets the final application and industry requirements. Therefore, PBF devices were originally designed for using one powder source at once only. Owing to the previously described advantages of MMAM, efforts were made in academia in the last years for developing PBF devices with the possibility of applying more than one powder type and manufacturing FGM with laser PBF (L-PBF) [12–17]. Wei et al. [18] gave a comprehensive overview of the different approaches of applying multiple powders in PBF processes and the respective characteristics. The strategy here is comparable to L-DED processes. The gradient is achieved by adjusting the chemical composition and the process parameter layer-wise. Unlike the L-DED processes, the layer thickness in PBF processes is small, resulting in the possibility of manufacturing a more continuous gradient if the increment of chemical composition difference of the feedstock material is small. However, for some material combinations with different base elements of the alloys, the interface between the layers may be discrete due to a lack of the *in-situ* mixing degree and a limited solubility of the materials, even in the case of PBF processes. Particular for the case of a small melt pool, which does not reach the lower layers with regarding the upper layer another chemical composition, the *in-situ* mixing degree is limited. Further limiting factor regarding *in-situ* mixing degree and thus a gradient is the liquid life time of the melt pool. Thus, for a continuous and smooth gradient with conventional *in-situ* mixing degree, many different powders need to be applied in one part. This is technically possible but not economical due to the necessity of extensions of contemporary PBF devices and additional effort regarding the management of much more powder sorts, including the investigation of process parameter for each powder.

2 State of the art

Marangoni convection is a material transport in liquid metals due to a difference in respective surface tensions resulting from a temperature gradient in the melt pool during processes, such as L-PBF, L-DED, welding, or any fusion-based processes with liquid interactions (Fig. 1(a)). Material transport by Marangoni convection reaches macroscopic range if the liquid lifetime and the melt pool size are sufficient. No homogeneous material distribution is expected. Another relevant method of material transport is atomistic diffusion. The driving force for thermal diffusion is the concentration gradient, as shown in Fig. 1(b). According to Fick's law of diffusion, the material transport via atomistic diffusion depends on the material combination-dependent diffusion coefficient, the concentration gradient, and the temperature. The range and extent of material transport by atomistic diffusion are less pronounced than those by Marangoni convection. Due to the concentration gradient being a driving force of diffusion, a homogenization of the material may be possible. Thus, the superposition of both effects resulting from a layer-wise remelting may be a suited approach to achieve the targeted enhancement of the mixing degree during AM in FGM, as shown in Figs. 1(c) and 1(d).

Laser remelting (LR) is a post-process applied on, e.g., electroplated, laser cladding, or thermal sprayed coatings. The aims are homogenization, grain refinement, and porosity reduction of the respective coatings [19–24]. In the past, several publications described the mentioned effects of LR on additive manufactured parts [25–27]. Xin et al. [25] described the influence of layer-wise LR on the microstructure and mechanical properties of thin-wall structures of 316L manufactured by L-DED. The application of LR resulted in increased average hardness and homogenization of the hardness values along the build-up direction. The supposed reason for the hardness increase was the stated reduction in the porosity by LR. Moreover, with LR-application the tensile properties were improved. In detail, the yield strength, the ultimate tensile strength, and the elongation could be increased by ~17%, ~19%, and ~59%, respectively. Li et al. [26] reported about the possibilities of grain refinement during a L-PBF process of a high-entropy alloy by adding nano TiN-reinforcement particles to the base powder and additional layer-wise LR. The TiN-nanoparticles were blended prior to the L-PBF process to the high-entropy alloy powder to promote grain refinement by providing nucleation sites during solidification. By applying LR, a more homogeneous distribution of the TiN-nanoparticles and an even higher effect of grain refinement were achieved, resulting in improved tensile properties compared with the case of without adding TiN-particles and adding TiN-particles but without applying LR. Some amorphous phases with different amorphization degrees were detected in the AM parts. Song et al. [27] investigated the influence of LR on the properties of 18Ni-300 maraging steel manufactured by L-PBF. The results showed that in dependence of the LR parameter, a reduction and an increase of porosity are possible. For the case of porosity reduction, the amount of pores increased whereas the size of the pores was significantly reduced, resulting in reduced total porosity value. Porosity reduction occurred due to (a) the improved surface quality of the respective layer, leading to a more uniform powder spreading when coating; and (b) the elimination of prior existing defects during LR by the Marangoni-driven melt flow. Since the porosity reference value without applying LR was below 1%, the porosity reduction due to LR showed no significant influence on the yield and ultimate tensile strength. The elongation, however, increased from 10.5% ± 0.8% in as-build condition to 13% ± 3.5% for the case of LR application. The authors supposed the reduced porosity and the stated formation of more nanoprecipitations to be responsible for the elongation increase when applying LR. In these publications, the emphasis was placed on the influence of LR on morphology formation and the mechanical properties of different monolithic alloys processed by AM with laser as energy source. However, no publications have discussed the influence of LR on the interface formation of MMAM parts processed with L-PBF at present. Thus, the present study focused on the influence of LR during MMAM, particularly on the interface formation and possible enhancement of the mixing degree.

3 Experiments

Experiments were conducted with an Aconity MINI device of Aconity3D (Herzogenrath, Germany). The L-PBF device was equipped with a 1000 W power and 200 μm spot-size laser. Argon with an oxygen content

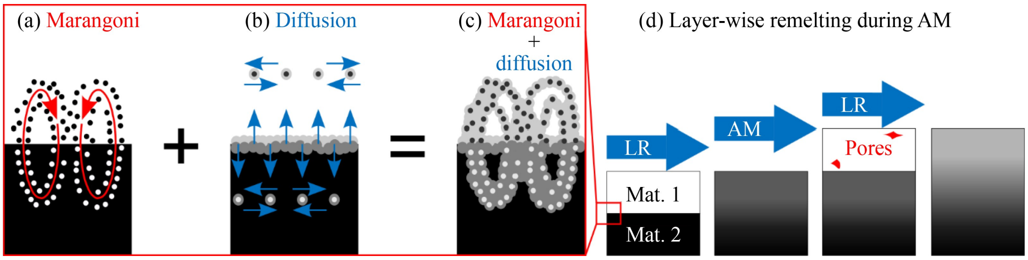

Fig. 1 Schematic of relevant effects: (a) Marangoni convection, (b) diffusion, (c) superposition of Marangoni convection and diffusion, and (d) layer-wise remelting during additive manufacturing (AM). Mat.: material, LR: laser remelting.

below 200 ppm O_2 was used as shielding gas. Due to the technical limitations of the used device, no preheating of the build plate was conducted. A low-alloyed steel, representing the first material, was chosen as the build plate material because the applied L-PBF device has only one powder container. Pure copper powder, representing the second material, with a particle size distribution of 15–45 μm was used as feedstock material. The chemical composition of the build plate and the copper powder as measured with EDX prior to L-PBF are stated in Table 1.

The process parameters are shown in Table 2. The process parameter set V1 was chosen on the basis of a previous study to improve process stability and the part properties for AM of copper with the used device. This parameter set represents the as-build condition and is used as reference for V2 and V3. The V2 and V3 parameter sets were chosen to evaluate the influence of LR or a higher energy density as alternative to LR on the mixing degree, respectively. V4 was selected as the LR effect parameter set for V3. Except in Table 2 stated parameter, the following parameters were constant. A layer thickness of s = 30 μm and a scan path distance of d = 100 μm were applied. For the samples with LR application, the same power and scan velocity as for the AM process were applied for every layer when remelting. The samples had a geometry of a cuboid with a base of A = 10 mm × 10 mm and a height of h = 2 mm. The samples were cut diagonally to obtain cross sections with sufficient size for the analyses. Subsequent scanning electron microscopic (SEM) analyses of the sample cross-sections, including energy dispersive X-ray (EDX) spectroscopy, were carried out on Phenom XL G2 (ThermoFisher Scientific, Waltham, USA).

Table 1 Chemical compositions of build plate and copper powder

Component	Fe/wt.%	Mn/wt.%	Cu/wt.%	Additional information
Build plate	Balance	2.6–3.4	0	Bulk material
Copper powder	0	0	100	Powder, 15–45 μm

4 Results and discussion

Figure 2 shows the SEM cross-sectional images of the sample manufactured with P = 800 W and v = 1000 mm/s and without LR application. Some pores are visible in the

Table 2 AM and LR process parameter

Sample	Power/W	Scan velocity/ $(\mathrm{mm \cdot s^{-1}})$	Remelting	Object
V1	800	1000	Not applied	Regarding AM process optimized parameter set: reference for V2 and V3
V2	800	1000	Applied, LR parameter same as AM	Influence of LR on V1 regarding mixing degree
V3	1000	1000	Not applied	Influence of higher energy density on V1 regarding mixing degree and reference for V4
V4	1000	1000	Applied, LR parameter same as AM	Influence of LR on V3 regarding mixing degree

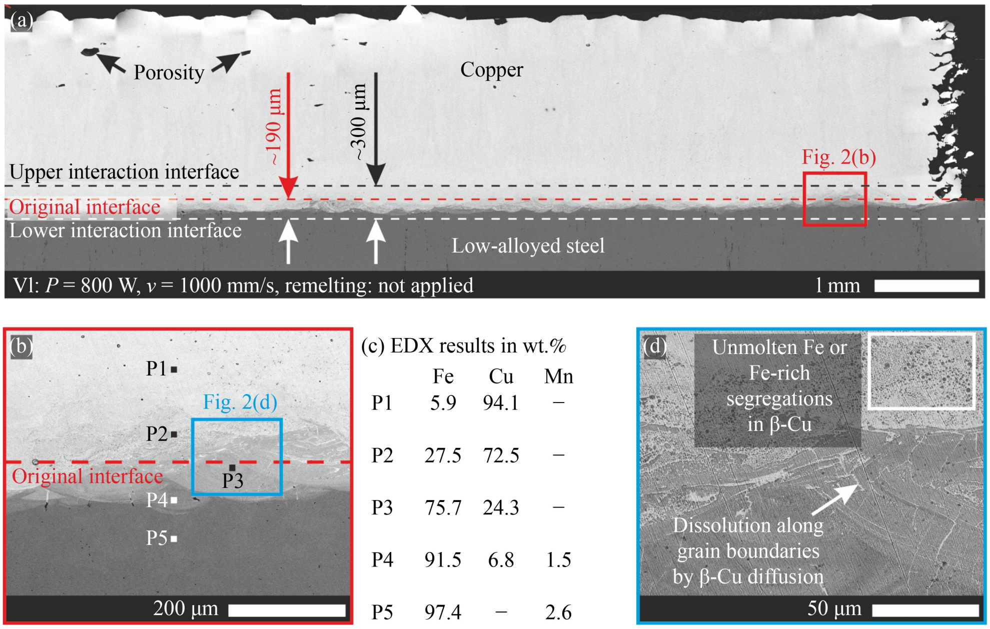

(c) EDX results in wt.%

	Fe	Cu	Mn
P1	5.9	94.1	–
P2	27.5	72.5	–
P3	75.7	24.3	–
P4	91.5	6.8	1.5
P5	97.4	–	2.6

Fig. 2 Scanning electron microscopic cross-sectional images of a sample manufactured with P = 800 W and v = 1000 mm/s and without laser remelting application and energy dispersive X-ray (EDX) spectroscopy results: (a) overview image, (b) detailed image indicating positions of EDX measurements, (c) EDX results in wt.%, and (d) detailed image of the interface.

copper AM part. Furthermore, pore formation occurred preferably in the upper layers of the sample. By carefully choosing the AM parameter, the porosity may be reduced further. The application of post processes, such as hot isostatic pressing, is another alternative for improving the porosity value. The maximal interaction distance which is the distance of the material transport by means of the Marangoni effect and thermal diffusion is $d \approx 300$ μm and varies along the interface, as shown in Fig. 2(a).

The visible material transport of copper into the steel base material was more pronounced than vice versa. In detail, the maximal penetration depth of copper into steel was about 190 μm and that of steel into the copper was about 110 μm. The penetration depth was irregular along the interface. According to the grey scales, five different morphologies with different chemical compositions were visible within the interaction zone between pure copper and the base material, as shown in Fig. 2(b). EDX measurements were performed in the regions depicted in Fig. 2(b) to evaluate the chemical composition, and the results are shown in Fig. 2(c). The base material contained $x_{\mathrm{Fe,P5}} = 97.4$ wt.% iron and $x_{\mathrm{Mn,P5}} = 2.6$ wt.% manganese, correlating with the chemical composition of the applied low alloy steel.

The iron–copper (Fe–Cu) phase diagram is characterized by a miscibility gap and a limited maximal solubility of copper and iron in the α-iron (α-Fe), γ-iron (γ-Fe), and the β-copper (β-Cu) phases, as shown in Fig. 3(a). Therefore, a chemical gradient can be adjusted only by a rising or a sloping fraction of segregations in the matrix. The iron fraction in the region P1 was $x_{\mathrm{Fe,P1}} = 5.9$ wt.%. Considering that the maximal solubility of iron in β-Cu phase was 4.1 wt.%, the high thermal cooling rates during the AM process may result in supersaturation of iron in the β-Cu in the case of P1. Furthermore, the EDX measurements showed a chemical composition of $x_{\mathrm{Fe,P2}} =$ 27.5 wt.% iron and $x_{\mathrm{Cu,P2}} = 72.5$ wt.% copper for the case of P2 region, and $x_{\mathrm{Fe,P3}} = 75.7$ wt.% iron and $x_{\mathrm{Cu,P3}} = 24.3$ wt.% copper for the case of P3 region. Given that the amount of iron in the β-Cu and of copper in the α- or γ-Fe was far above the maximal solubility of the respective phases, the supersaturation was assumed to be not the

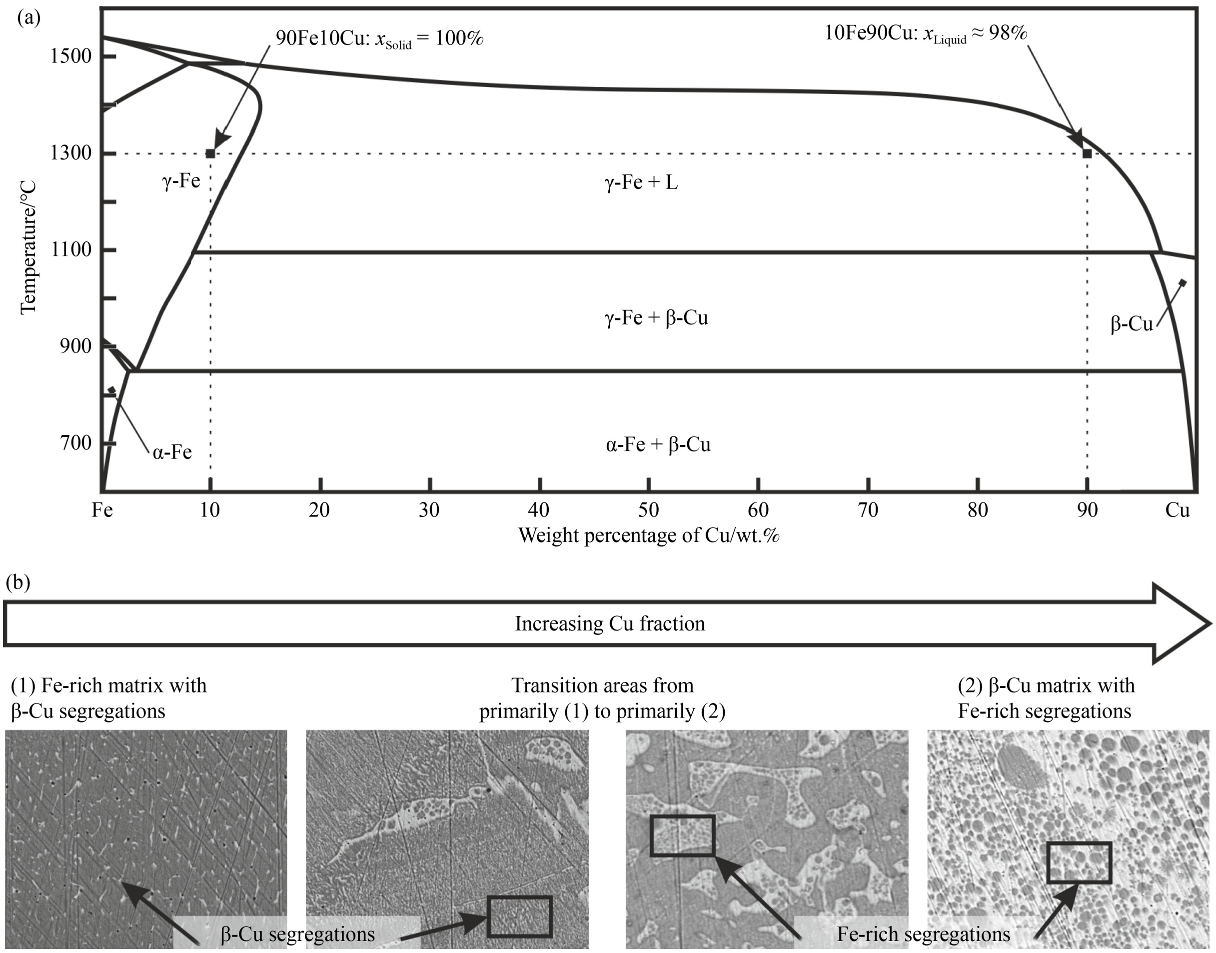

Fig. 3 (a) Fe–Cu phase diagram according to Ref. [28] indicating the liquid fraction at a temperature of $T = 1300$ °C in dependence of the local chemical composition and (b) scanning electron microscopic images indicating the phase formation with the influence of the local chemical composition.

reason for the present morphology and chemical composition. In fact, the formation of the present interaction zone is more complex and is supposed to result from a superposition of different metallurgical effects. In detail, next to the Marangoni effect and thermal diffusion, particularly along the grain boundaries, segregations are supposed to be the relevant effects resulting in the present morphology and the respective chemical compositions. Thus, during the solidification of initially homogenous liquid Cu–Fe alloy, segregations of β-Cu in the Fe-rich matrix and vice versa may be formed when the respective temperature-dependent solubility limit is undercut (Fig. 3(b)). Furthermore, particularly within the thixotropic temperature range and thus during the melting or solidification process, the Marangoni convection is supposed to distribute either the solidified segregations or un-melted base material iron in the liquid matrix, resulting in the present morphology. Lastly, in the case of liquid copper, the microscopic diffusion along grain boundaries resulting in the dissolution of Fe-rich phases by β-Cu is a relevant effect, enhancing the copper amount in a macroscopic homogenous Fe-rich matrix (Fig. 2(d)).

Figure 4(a) shows an overview of the SEM cross-sectional image of the sample manufactured with P = 800 W, v = 1000 mm/s, and LR application for every layer. A visual comparison of V2 to V1 showed that the porosity was lower when applying LR. This finding correlates with state of the art. The interface between the unmolten base material and the interaction zone was more irregular than in the case of no LR application. The maximal interaction distance and penetration depth were $d \approx 610$ and 350 μm, respectively, and they varied along the interface. Therefore, by applying LR, the maximal interaction zone thickness and the penetration depth was doubled, resulting in a higher mixing degree and thus, in a smoother gradient between the base material and the AM part. However, the deviation of the mixing degree and the continuity of the gradient varied along the interface. Figure 4(b) shows a detailed SEM image of the interaction zone and depicts the regions of the conducted EDX measurements. The EDX results indicated a smoother gradient of the chemical composition, particularly for the regions P1–P5, as illustrated in Fig. 4(c). These regions were characterized by a β-Cu matrix with graded amount of Fe-rich segregations, as shown in Fig. 5. According to the EDX spot measurements, the fraction of copper in the Fe-rich segregations varied in the range of 20 wt.% < x_{Cu} < 30 wt.% and is thus above the chemical composition of γ-Fe. The positions of the

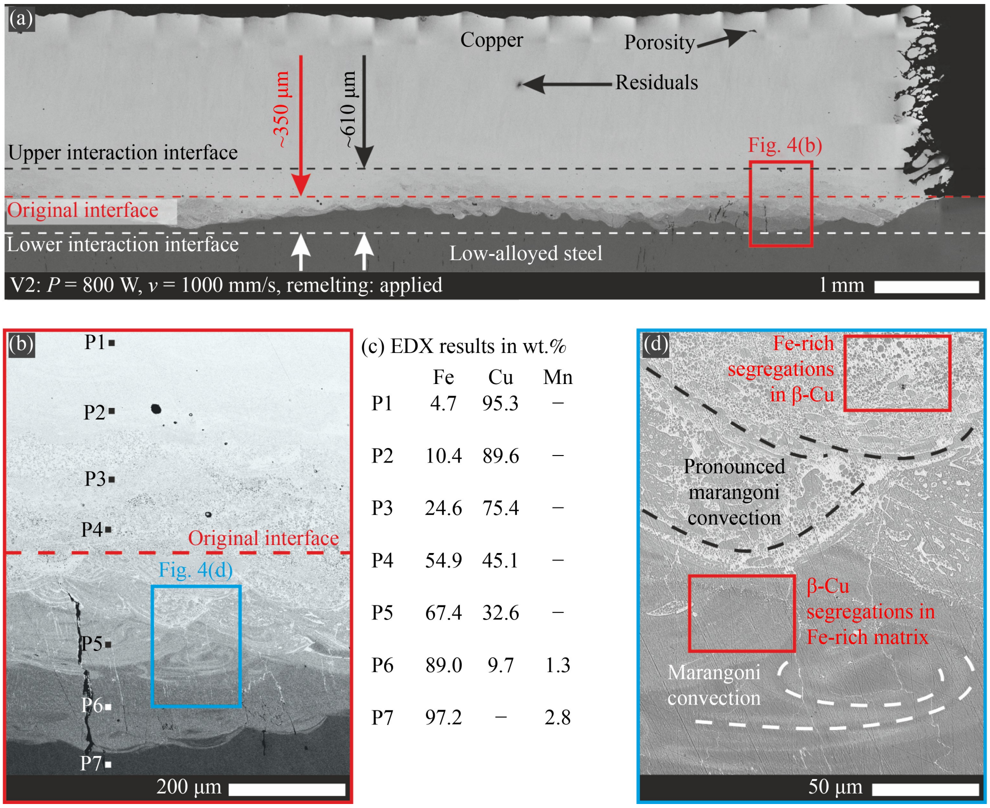

(c) EDX results in wt.%

	Fe	Cu	Mn
P1	4.7	95.3	–
P2	10.4	89.6	–
P3	24.6	75.4	–
P4	54.9	45.1	–
P5	67.4	32.6	–
P6	89.0	9.7	1.3
P7	97.2	–	2.8

Fig. 4 Scanning electron microscopic cross-sectional images of sample manufactured with P = 800 W, v = 1000 mm/s, and laser remelting application and energy dispersive X-ray (EDX) spectroscopy results: (a) overview image, (b) detailed image indicating positions of EDX measurements, (c) EDX results in wt.%, and (d) detailed image of the interface indicating Marangoni convection.

conducted EDX spot measurements of Fe-rich segregations are marked with a red circle in Fig. 5.

Starting from the interface between P5 and P6 and thus the regions with Fe-rich matrix, the gradient was less continuous, and discrete interfaces were visible. Considering that the liquidus temperature of the relevant Fe-rich phase was higher and the liquid fraction was lower than that of β-Cu, the liquid lifetime of the Fe-rich matrix regions is supposed to be smaller, resulting in a lower effect of Marangoni convection regarding the mixing degree, as shown in Fig. 3(a). Figure 4(d) indicates a higher effect of the Marangoni convection in the region with the β-Cu matrix than in the region with Fe-rich matrix. The Marangoni effect was evaluated from the grayscales of the corresponding phases, and their distribution and the turbulences corresponding to the melt flow. In detail, the turbulences and the melt flow were aligned horizontally and less pronounced in the case of the Fe-rich matrix. For the case of β-Cu matrix, the turbulences, which indicate the melt flow, were aligned horizontally and vertically and more pronounced. Regions with a pronounced Marangoni flow were characterized by a local higher mixing degree, resulting in a local higher ratio of copper to iron for the case of regions below the original interface.

Figure 6 shows the SEM cross-sectional images of the sample manufactured with P = 1000 W and v = 1000 mm/s and without LR application and the EDX results. Figure 6(a) shows an overview of the SEM cross-sectional image of the sample manufactured with P = 1000 W and v = 1000 mm/s and without LR application. By the higher energy density, the melt pool temperature and size and the effect of Marangoni convection enhanced compared with those in V1. This finding resulted in a maximal interaction distance of $d \approx 410$ μm. The maximal penetration depth was about 240 μm, and it varied along the interface. However, the maximal interaction distance and the penetration depth were lower than in the case of V2. The upper surface roughness was higher than in the case of V1 or V2. Although a higher energy density was applied, the porosity was significantly higher than that in V1 or V2. Furthermore, some unmelted powder was entrapped in the pores, as shown in Fig. 6(d). According to Refs. [29–31], this effect may result from the keyhole mode or of an excessively pronounced Marangoni convection. The keyhole mode is characterized by material evaporation and may result in pore formation. Furthermore, high energy density results in excessively pronounced Marangoni convection, and thus, the pronounced melt pool dynamic drags some un-

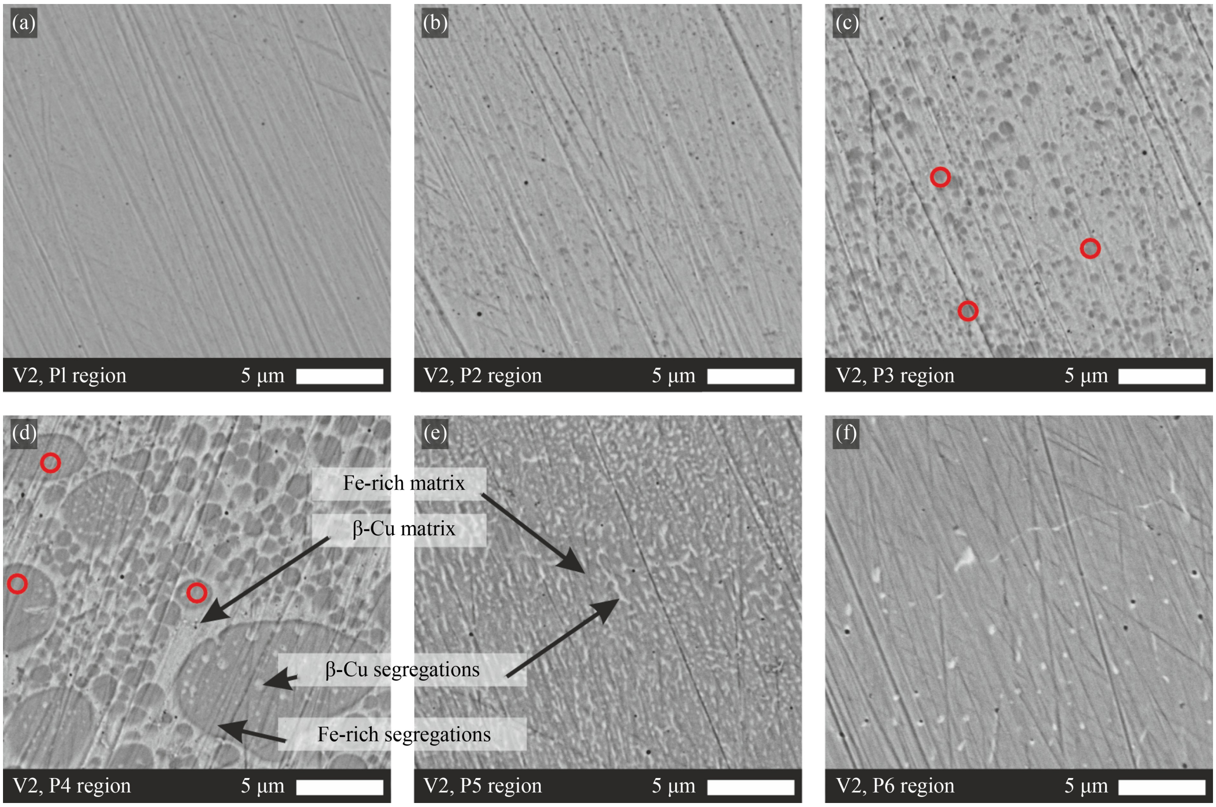

Fig. 5 Detailed scanning electron microscopic images of regions with conducted energy dispersive X-ray (EDX) spectroscopy area measurements regarding Fig. 4(b) of the sample V2, (a) P1 region, (b) P2 region, (c) P3 region indicating positions of EDX spot measurements, (d) P4 region indicating positions of EDX spot measurements, (e) P5 region, and (f) P6 region.

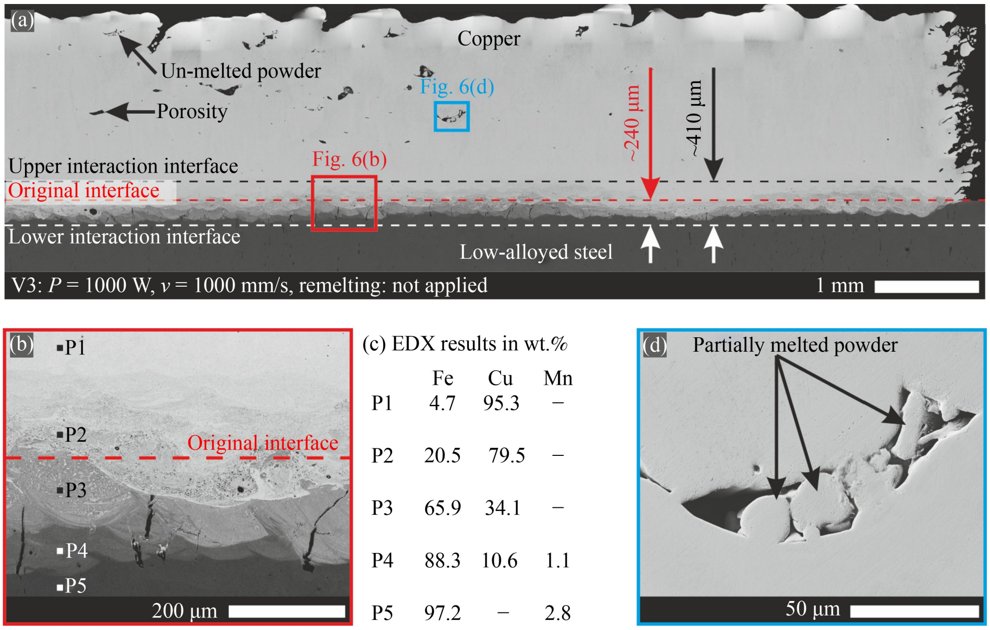

(c) EDX results in wt.%

	Fe	Cu	Mn
P1	4.7	95.3	–
P2	20.5	79.5	–
P3	65.9	34.1	–
P4	88.3	10.6	1.1
P5	97.2	–	2.8

Fig. 6 Scanning electron microscopic cross-sectional images of sample manufactured (with $P = 1000$ W and $v = 1000$ mm/s and without laser remelting application) and energy dispersive X-ray (EDX) spectroscopy results: (a) overview image, (b) detailed image indicating positions of EDX measurements, (c) EDX results in wt.%, and (d) detailed image of a pore with entrapped partially melted powder.

melted side particles into the melt pool. Due to the present high cooling rates and short liquid lifetime, the particles remained completely or partially un-melted once the melt pool around solidified. Therefore, when melting the powder for the first time, the *in-situ* mixing degree is limited by the keyhole mode and an excessively melt pool dynamic due to excessive Marangoni convection resulting in the formation of pores. Thus, using a parameter set with higher energy densities is not appropriate to achieve pore free and high-quality FGM. Figure 6(b) shows a detailed SEM image of the interaction zone and depicts the regions of the conducted EDX measurements. The EDX results indicated a smoother gradient than that in V1 but a less smooth gradient than that in V2, as shown in Fig. 6(c).

Figure 7 shows an overview of the SEM cross-sectional image of the sample manufactured with $P = 1000$ W, $v = 1000$ mm/s, and LR application. Compared with those in V3, the upper surface roughness and porosity were improved by applying LR. Furthermore, by applying LR, the interaction distance and the penetration depth were increased. In detail, the maximal interaction distance was $d = 750$ μm, and the maximal penetration depth was about 440 μm, indicating a higher mixing degree, and thus, a smoother gradient. Figure 7(b) shows a detailed SEM image of the interaction zone and depicts the regions of the EDX measurements. For the regions P1–P5, the gradient was found to be the smoothest among other samples, as shown in Fig. 7(c). The interface between the regions P6 and P7 was discrete.

5 Summary and conclusions

The Marangoni convection was shown to be the main driving force for the material transport in the melt pool during the AM process. Next to the Marangoni convection, thermal diffusion was supposed to be a relevant effect concerning local homogenization of the chemical composition. On the one hand, applying high energy densities during the first-time melting of the powder enhanced the mixing degree. On the other hand, high energy densities influenced the quality of the AM part negatively by promoting the formation of pores in general and pores with entrapped un-melted or partially melted powder. This finding was supposed to be due to the excessively pronounced melt pool dynamic dragging side powder particles into the melt pool, suggesting that with regard on the quality of the AM part, the possible maximal mixing degree is limited during one-time melting.

Therefore, LR application is necessary to enhance the mixing degree in a controlled manner without lowering the quality of the AM part. The LR experiments showed that the interaction distance and the penetration depth were enhanced approximately by two times, resulting in a smoother gradient. In this context, Fig. 8 shows the distribution of Fe and Cu in depth direction (*Z*-axis) starting from the original interface. The mixing of the elements in depth direction was clearly more pronounced (factor 2) when using the LR process. As a side effect, the porosity of the AM parts and the upper surface roughness improved, which correlates with the state of the art.

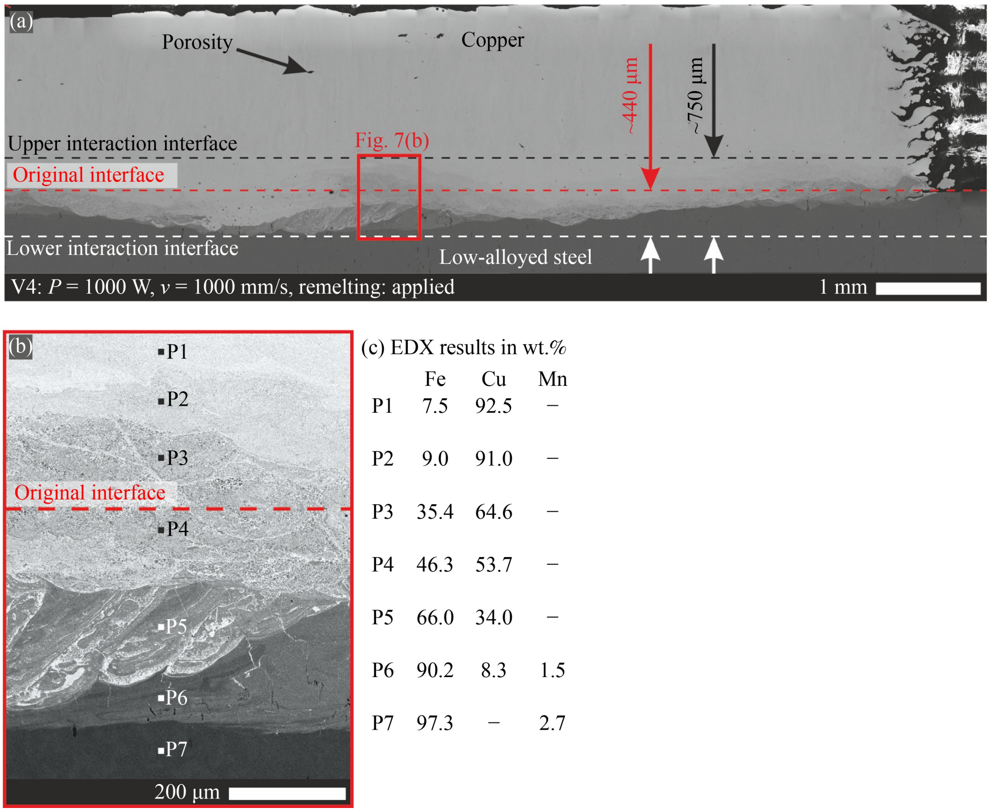

(c) EDX results in wt.%

	Fe	Cu	Mn
P1	7.5	92.5	–
P2	9.0	91.0	–
P3	35.4	64.6	–
P4	46.3	53.7	–
P5	66.0	34.0	–
P6	90.2	8.3	1.5
P7	97.3	–	2.7

Fig. 7 Scanning electron microscopic cross-sectional images of sample manufactured with P = 1000 W, v = 1000 mm/s, and laser remelting application and energy dispersive X-ray (EDX) spectroscopy results: (a) overview image, (b) detailed image indicating positions of EDX measurements, and (c) EDX results in wt.%.

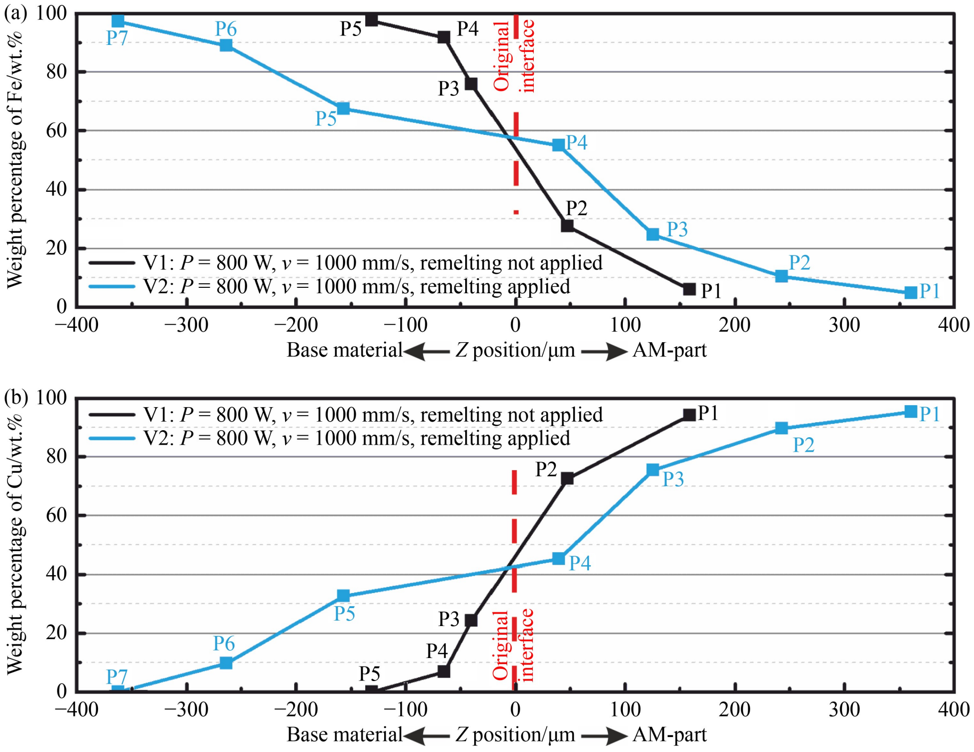

Fig. 8 Estimated chemical composition along Z-axis of V1 and V2 according to conducted energy dispersive X-ray spectroscopy measurements: weight percentages of (a) Fe and (b) Cu. AM: additive manufacturing.

Therefore, layer-wise LR application is a promising approach to achieve a sufficient mixing degree resulting in a continuous gradient and a high-quality part simultaneously. Each technology has advantages and disadvantages when comparing the presented approach with the state of the art and namely blending powders in L-DED and L-PBF processes. For the case, the gradation quality of the chemical composition between two layers is the decisive criterion for technology selection the presented LR-approach fulfils the requirements in a higher degree. For the case, a specific step-like gradient with no regard on the formation of the interface between two layers is sufficient the approaches with applied blended powders are more economical due to the necessity of one-time melting in each layer only. Furthermore, the LR approach and the approach of applying different or blended powders complement each other.

Nomenclature

AM	Additive manufacturing
EDX	Energy dispersive X-ray
FGM	Functionally graded material
L-DED	Laser-directed energy deposition
L-PBF	Laser powder bed fusion
LR	Laser remelting
MMAM	Multi-material additive manufacturing
PBF	Powder bed fusion
SEM	Scanning electron microscopic

Funding Note Open Access funding enabled and organized by Projekt DEAL.

Conflict of Interest The authors declare that they have no conflict of interest.

References

1. Kieback B, Neubrand A, Riedel H. Processing techniques for functionally graded materials. Materials Science and Engineering: A, 2003, 362(1–2): 81–106
2. Tillmann W, Lopes Dias N F, Stangier D. Influence of plasma nitriding pretreatments on the tribo-mechanical properties of DLC coatings sputtered on AISI H11. Surface and Coatings Technology, 2019, 357: 1027–1036
3. Maile K, Berreth K, Lyutovich A. Functionally graded coatings of carbon reinforced carbon by physical and chemical vapour deposition (PVD and CVD). Materials Science Forum, 2005, 492–493: 347–352
4. Sam M, Jojith R, Radhika N. Progression in manufacturing of functionally graded materials and impact of thermal treatment—a critical review. Journal of Manufacturing Processes, 2021, 68: 1339–1377
5. Sobczak J J, Drenchev L. Metallic functionally graded materials: a specific class of advanced composites. Journal of Materials Science and Technology, 2013, 29(4): 297–316
6. Tammas-Williams S, Todd I. Design for additive manufacturing with site-specific properties in metals and alloys. Scripta Materialia, 2017, 135: 105–110
7. Reichardt A, Shapiro A A, Otis R, Dillon R P, Borgonia J P, McEnerney B W, Hosemann P, Beese A M. Advances in additive manufacturing of metal-based functionally graded materials. International Materials Reviews, 2021, 66(1): 1–29
8. Knoll H, Ocylok S, Weisheit A, Springer H, Jägle E, Raabe D. Combinatorial alloy design by laser additive manufacturing. Steel Research International, 2017, 88(8): 1600416
9. Li W, Karnati S, Kriewall C, Liou F, Newkirk J, Brown Taminger K M, Seufzer W J. Fabrication and characterization of a functionally graded material from Ti−6Al−4V to SS316 by laser metal deposition. Additive Manufacturing, 2017, 14: 95–104
10. Domack M S, Baughman J M. Development of nickel−titanium graded composition components. Rapid Prototyping Journal, 2005, 11(1): 41–51
11. Ocylok S, Weisheit A, Kelbassa I. Functionally graded multi-layers by laser cladding for increased wear and corrosion protection. Physics Procedia, 2010, 5: 359–367
12. Demir A G, Previtali B. Multi-material selective laser melting of Fe/Al−12Si components. Manufacturing Letters, 2017, 11: 8–11
13. Scaramuccia M G, Demir A G, Caprio L, Tassa O, Previtali B. Development of processing strategies for multigraded selective laser melting of Ti6Al4V and IN718. Powder Technology, 2020, 367: 376–389
14. Tey C F, Tan X P, Sing S L, Yeong W Y. Additive manufacturing of multiple materials by selective laser melting: Ti-alloy to stainless steel via a Cu-alloy interlayer. Additive Manufacturing, 2020, 31: 100970
15. Wei C, Sun Z, Chen Q, Liu Z, Li L. Additive manufacturing of horizontal and 3D functionally graded 316L/Cu10Sn components via multiple material selective laser melting. Journal of Manufacturing Science and Engineering, 2019, 141(8): 081014
16. Niendorf T, Leuders S, Riemer A, Brenne F, Tröster T, Richard H A, Schwarze D. Functionally graded alloys obtained by additive manufacturing. Advanced Engineering Materials, 2014, 16(7): 857–861
17. Nadimpali V K, Dahmen T, Valente E H, Mohanty S, Pedersen D

B. Multi-material additive manufacturing of steels using laser powder bed fusion. In: Proceedings of the 19th International Conference & Exhibition. Bilbao: DTU Library, 2019, 240–243

18. Wei C, Zhang Z Z, Cheng D X, Sun Z, Zhu M H, Li L. An overview of laser-based multiple metallic material additive manufacturing: from macro- to micro-scales. International Journal of Extreme Manufacturing, 2021, 3(1): 012003
19. Yang K, Li J Q, Wang Q Y, Li Z Y, Jiang Y F, Bao Y F. Effect of laser remelting on microstructure and wear resistance of plasma sprayed Al_2O_3−40%TiO_2 coatings. Wear, 2019, 426–427: 314–318
20. Cui C, Ye F X, Song G R. Laser surface remelting of Fe-based alloy coatings deposited by HVOF. Surface and Coatings Technology, 2012, 206(8–9): 2388–2395
21. Li Y L, Song P, Wang W Q, Lei M, Li X W. Microstructure and wear resistance of a Ni−WC composite coating on titanium grade 2 obtained by electroplating and electron beam remelting. Materials Characterization, 2020, 170: 110674
22. Lima M S F, Folio F, Mischler S. Microstructure and surface properties of laser-remelted titanium nitride coatings on titanium. Surface and Coatings Technology, 2005, 199(1): 83–91
23. Serres N, Hlawka F, Costil S, Langlade C, Machi F. Microstructure and environmental assessment of metallic NiCrBSi coatings manufactured via hybrid plasma spray process. Surface and Coatings Technology, 2010, 205(4): 1039–1046
24. Li R F, Jin Y J, Li Z G, Zhu Y Y, Wu M F. Effect of the remelting scanning speed on the amorphous forming ability of Ni-based alloy using laser cladding plus a laser remelting process. Surface and Coatings Technology, 2014, 259: 725–731
25. Xin B, Zhou X X, Cheng G, Yao J, Gong Y D. Microstructure and mechanical properties of thin-wall structure by hybrid laser metal deposition and laser remelting process. Optics & Laser Technology, 2020, 127: 106087
26. Li B, Zhang L, Yang B. Grain refinement and localized amorphization of additively manufactured high-entropy alloy matrix composites reinforced by nano ceramic particles via selective-laser-melting/remelting. Composites Communications, 2020, 19: 56–60
27. Song J, Tang Q, Feng Q X, Han Q Q, Ma S, Chen H, Guo F Y, Setchi R. Effect of remelting processes on the microstructure and mechanical behaviours of 18Ni-300 maraging steel manufactured by selective laser melting. Materials Characterization, 2022, 184: 111648
28. Okamoto H, Schlesinger M E, Müller E M. ASM Handbook: Alloy Phase Diagrams. ASM International, 1992
29. Khairallah S A, Anderson A T, Rubenchik A, King W E. Laser powder-bed fusion additive manufacturing: physics of complex melt flow and formation mechanisms of pores, spatter, and denudation zones. Acta Materialia, 2016, 108: 36–45
30. Sun Z, Chueh Y H, Li L. Multiphase mesoscopic simulation of multiple and functionally gradient materials laser powder bed fusion additive manufacturing processes. Additive Manufacturing, 2020, 35: 101448
31. Chen C Y, Gu D D, Dai D H, Du L, Wang R, Ma C L, Xia M J. Laser additive manufacturing of layered TiB2/Ti6Al4V multi-material parts: understanding thermal behavior evolution. Optics & Laser Technology, 2019, 119: 105666